WILEY-VCH

DOI: 10.1002/solr.201800095
Article type: Full Paper

Charge photogeneration and recombination in mesostructured CuSCN-nanowire/$PC_{70}BM$ solar cells

Yuliar Firdaus, Akmaral Seitkhan, Flurin Eisner, Wai-Yu Sit, Zhipeng Kan, Nimer Wehbe, Ahmed H. Balawi, Emre Yengel, Safakath Karuthedath, Frédéric Laquai, Thomas D. Anthopoulos**

Dr. Y. Firdaus, A. Seitkhan, Dr. Z. Kan, A. H. Balawi, Dr. E. Yengel, Dr. S. Karuthedath

Assoc. Prof. F. Laquai, Prof. T. D. Anthopoulos

King Abdullah University of Science and Technology (KAUST)

KAUST Solar Center, Division of Physical Sciences and Engineering

Thuwal 23955-6900, Saudi Arabia

E-mail: yuliar.firdaus@kaust.edu.sa; thomas.anthopoulos@kaust.edu.sa

Dr. N. Wehbe

King Abdullah University of Science and Technology (KAUST)

Core Lab, Thuwal, 23955-6900, Saudi Arabia

F. Eisner, W-Y. Sit, Prof. T. D. Anthopoulos

Department of Physics, Imperial College London

South Kensington, London SW7 2AZ (UK)

Keywords: Solar cells; Copper (I) thiocyanate; PCBM; charge photogeneration; charge recombination

Abstract

Fullerene-based materials are widely used as electron acceptors in organic bulk-heterojunction solar cells; yet, they have rarely been used as the only photoactive component due to their low absorbance and limited charge generation efficiency. However, blending the wide-bandgap *p*-type material copper (I) thiocyanate (CuSCN) with [6,6]-phenyl-C71-butyric acid methyl ester ($PC_{70}BM$) leads to the formation of a unique mesostructured *p*-*n* like heterointerface between CuSCN and $PC_{70}BM$ and solar cells with a power conversion efficiency (PCE) of up to 5.4%. Here, we examine in detail the reasons for the surprisingly high device performance and elucidate the charge photogeneration and recombination mechanisms in CuSCN-based devices with $PC_{70}BM$ as the exclusive light-absorbing material. Our studies clearly demonstrate that a substantial fraction of the photocurrent in the CuSCN-based devices results from improved dissociation of fullerene excitons and efficient charge transfer at the CuSCN:$PC_{70}BM$ interface combined with reduced geminate and nongeminate charge recombination losses. Our results have implications beyond the fullerene-based devices studied here, as they demonstrate that careful selection of a mesostructured *p*-type transparent semiconductor paves the path to a new type of efficient single photoactive material solar cells.

1. Introduction

The extent of progress in the development of organic bulk heterojunction (BHJ) solar cells has been tremendous and power conversion efficiencies (PCE) of over 13% have recently been achieved,[1, 2] owing to the development of nonfullerene acceptors in the past three years. Nonfullerene acceptors are set to outperform their fullerene counterparts as they exhibit great tunability of absorption spectra and energy levels.[1-6] However, due to their excellent transport

properties[7-9] combined with good solubility and miscibility when paired with selected donor materials,[10, 11] fullerene derivatives such as phenyl-C_{60}-butyric acid methyl ester ($PC_{60}BM$) or its C_{70} analogue ($PC_{70}BM$) are still being used extensively in organic photovoltaic research and investigation of this class of acceptors remains relevant.

Recently, it has been acknowledged that fullerene (C_{60}) and its derivatives not only play a key role as electron-acceptor and electron–transport materials in BHJs, but also contribute significantly to photon absorption and photocurrent generation.[12-17] In some cases, such as PCDTBT:$PC_{70}BM$, it has been proposed that light absorption in the $PC_{70}BM$ is the primary pathway for charge generation.[16] In fact, photogeneration in neat fullerene films has been discussed extensively.[15, 18-22] Chow et al. observed that upon photoexcitation of $PC_{60}BM$ and $PC_{70}BM$ films efficient intersystem crossing (ISC) of the fullerene singlet excitons to triplet excitons within 1 ns occurs,[21] however, no significant contribution of such triplet excitons to the photocurrent generation in OPV devices was reported.[23, 24] Keiderling et al. reported that excitation of $PC_{60}BM$ aggregates results in a substantial generation of intermolecular charge-transfer (CT) states, leading to charge generation.[19] Such intermolecular CT states have been reported as a source of the intrinsic photocurrent of fullerene films.[18, 20] These CT states, formed by electron transfer between the fullerene molecules, have a bandgap of 2.3-4.0 eV,[18, 20] which is significantly larger than the intramolecular Frenkel exciton bandgap of 1.5-1.9 eV.[20, 22] Hahn et al. further explained that for the case of C_{60} and $PC_{60}BM$ films, an intrinsic photogeneration occurs above a photon energy of

2.2-2.3 eV due to charges, which overcome their Coulomb attraction by an Onsager-like separation process facilitated by efficient coupling of CT states to charge transport states.[15] In fact, the binding energy of the CT state is much smaller than that of the Frenkel excitons in a fullerene and the photogenerated CT states can be separated at a relatively weak electric field.[25]

In our recent work, we have shown that functional solar cells can be prepared using $PC_{70}BM$ as the only absorber material, reaching PCEs up to 1% when using a bilayer CuSCN/$PC_{70}BM$ structure, while PCEs of over 5.4% were obtained, when CuSCN was mixed with the photoactive component, creating mesostructure CuSCN nanowires.[7] These solar cells provide a unique platform to study charge photogeneration and recombination in the fullerene phase and to investigate the role of the mesostructured interface. Thus, we examine the influence of the CuSCN interface on the charge photogeneration and recombination of CuSCN:$PC_{70}BM$ devices. Our detailed device studies show that improvements observed in the mixed CuSCN:$PC_{70}BM$ cells result from notably improved charge generation, reduced geminate, and reduced nongeminate recombination losses. Key to this improvement is the presence of a spontaneously-formed mesostructured interface of CuSCN nanowires and $PC_{70}BM$. We show that a greater proportion of the photocurrent in the CuSCN-based devices comes from the dissociation of photogenerated excitons and charge transfer at the CuSCN:$PC_{70}BM$ interface.

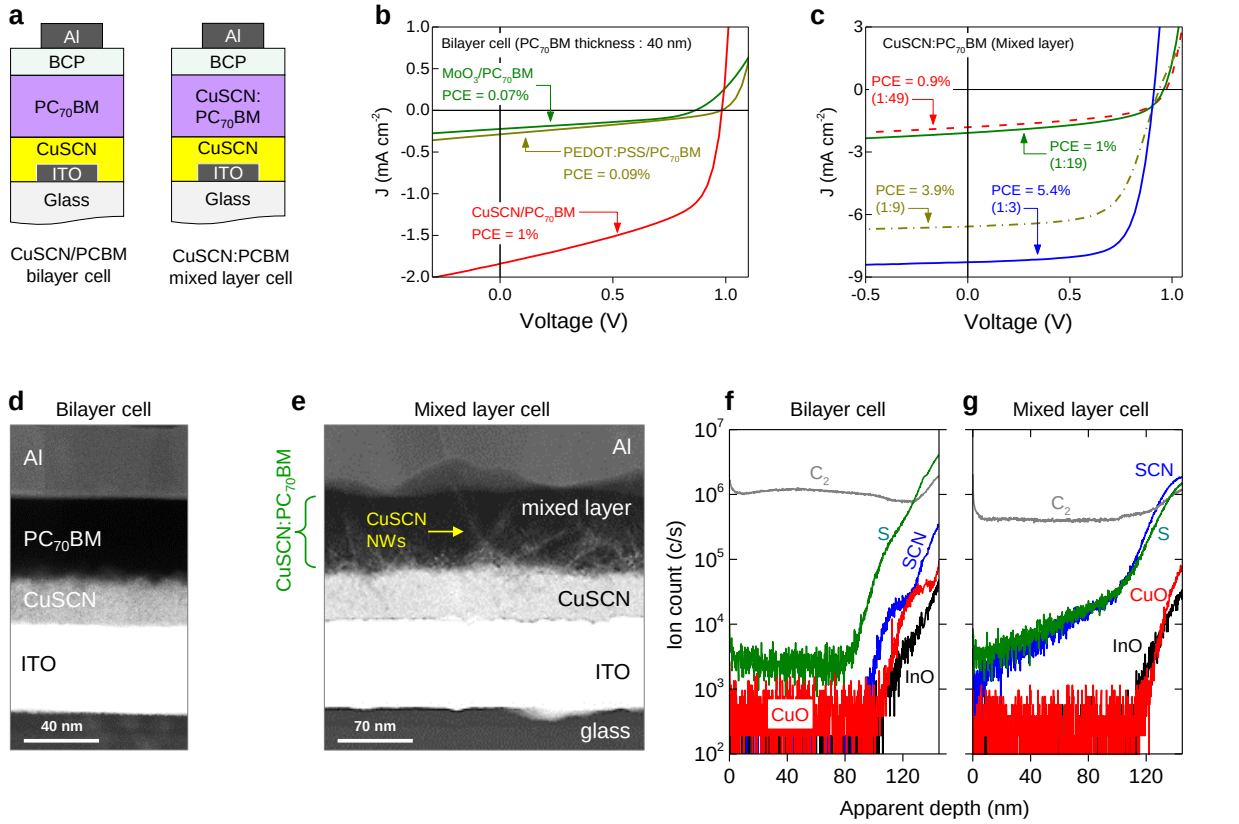

Figure 1. a) Schematics of device architectures of a bilayer CuSCN/$PC_{70}BM$ (left) and a mixed layer CuSCN:$PC_{70}BM$ (right) solar cell. b) *J-V* characteristics of bilayer CuSCN/$PC_{70}BM$ solar cells with optimized $PC_{70}BM$ layer thickness (40 nm); also shown for comparison MoO_3 and PEDOT:PSS-based devices (ITO/MoO_3 or PEDOT:PSS/$PC_{70}BM$/BCP/Al). c) *J-V* characteristics of mixed-layer CuSCN:$PC_{70}BM$ solar cells with different CuSCN:$PC_{70}BM$ ratios (by weight). d) High-resolution cross-sectional transmission electron microscopy (TEM) images of a bilayer CuSCN/$PC_{70}BM$ cell. e) TEM image of a mixed layer CuSCN/$PC_{70}BM$ cell. D-SIMS profiles for f) bilayer CuSCN/$PC_{70}BM$ (left) and g) mixed CuSCN/$PC_{70}BM$ (right) solar cell.

2. Results and Discussion

We begin our discussion by examining the device performance of the bilayer and mixed layer solar cells (**Figure 1a**). In both cells, CuSCN was chosen as the hole transport layer (HTL) and bathocuproine (BCP) as the electron transport layer (ETL) due to their excellent electron and hole

blocking properties, respectively. **Figure 1b** shows the current density-voltage (*J-V*) characteristics for bilayer CuSCN/$PC_{70}BM$ solar cells with an optimized $PC_{70}BM$ thickness (40 nm). The bilayer cell exhibits a maximum PCE up to 1% with a high V_{OC} of 0.99 V (FF = 55% and J_{SC} = 1.8 mA cm^{-2}). For comparison, the *J-V* characteristics of cells with MoO_3 and PEDOT:PSS as HTL are also shown in **Figure 1b**. Compared to cells employing CuSCN as HTL, the MoO_3 and PEDOT:PSS–based cells exhibit both markedly lower FF and $J_{SC,}$ resulting in PCEs of less than 0.1% (for device statistics see **Table S1**, Supporting information). While this large discrepancy between the devices can partly be explained by the superior electron and exciton blocking capabilities of CuSCN,[26, 27] the much higher *J*sc suggests that charge generation may also be more efficient in these devices. **Figure 1c** shows the *J-V* characteristics of the mixed layer device for different ratios of CuSCN to $PC_{70}BM$ (for device statistics see **Table S1**). For a ratio of 1:19 the average J_{SC} is only slightly increased to 2.1 mA cm^{-2}, resulting in a PCE ≈ 1% similar to the bilayer CuSCN/$PC_{70}BM$ device. The J_{SC} starts to increase significantly to 6.5 mA cm^{-2} when the ratio is 1:9 and reaches over 7.9 mA cm^{-2} for a CuSCN:$PC_{70}BM$ ratio of 1:3 (optimized condition). In general, the V_{OC} of the mixed cells (e.g. V_{OC} = 0.91 V for ratio 1:3) is lower than that of the bilayer cell (V_{OC} = 0.98 V) and close to the built-in voltages (V_{bi}: 0.88 V and 0.96 V for mixed and bilayer cells, respectively) as inferred from a Mott-Schottky analysis (**Figure S1**).[28] Preliminary study of the shelve lifetime of optimised CuSCN:PC70BM (1:3) cells revealed that when stored in nitrogen atmosphere at 21°C their performance characteristics remained stable of

up to four days without any noticeable degradation. However, when the same cells were exposed to ambient air (≈55% relative humidity) for a similar time duration, the cell's PCE was reduced by approximately 20% of its initial value. Detailed analysis of the operating stability of bilayer and mesistructured CuSCN:PC70BM solar cells will be reported in the future.

By comparing the cross-sectional TEM images of the bilayer and mixed layer cells (**Figure 1d** and **1e**), it is clear that the presence of the spontaneously-formed CuSCN nanowires is the main reason for the significant increase of the photocurrent in the mixed layer cells, as established in our previous work[7]. Further measurements of the active layer composition of the bilayer and mixed layer devices using dynamic secondary-ion mass spectrometry (D-SIMS) are in agreement with the cross-sectional TEM data. In particular, **Figure 1f** shows the D-SIMS depth profiles of these cells (without the top contact BCP/Al being present). The traces associated with SCN-groups contents (also S-atomic content) indicate a gradual concentration increase in CuSCN for the mixed CuSCN:$PC_{70}BM$ cell starting from the top of the active layer (left side) to the ITO interface (right side). On the other hand, the CuSCN content in the bilayer cell appears to increase abruptly, starting from a depth of 80 nm towards the ITO interface. The gradual increase of the CuSCN concentration towards the ITO side in the mixed cell is reminiscent of vertical segregation of donor and acceptor materials in BHJ solar cells.[29-31]

$PC_{70}BM$ has been known to have a significantly higher absorption coefficient than $PC_{60}BM$ due to its lower symmetry.[32, 33] To better quantify the optical absorption characteristics of $PC_{70}BM$,

we performed ellipsometry measurements. **Figure 2a** shows the extinction coefficient of CuSCN, $PC_{70}BM$, mixed CuSCN:$PC_{70}BM$, and P3HT:$PC_{70}BM$ (as reference) films inferred from thin-film ellipsometry. $PC_{70}BM$ film absorbs effectively between 350-600 nm with a respectable extinction coefficient (k≈0.4), while P3HT:$PC_{70}BM$ has a higher extinction coefficient from 450-650 nm (k≈0.6 at 500 nm) due to the contribution from P3HT. In contrast, mixing the $PC_{70}BM$ with CuSCN in the mixed phase CuSCN:$PC_{70}BM$ films (ratio 1:3) result in lower extinction coefficient than the pristine $PC_{70}BM$ film, as CuSCN provides a negligible contribution to the absorption above 350 nm.

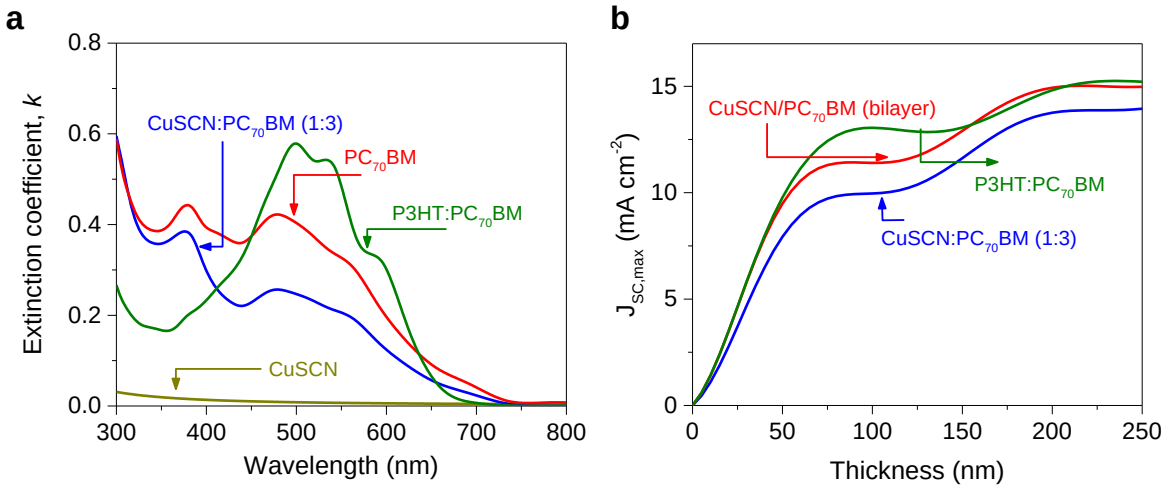

Figure 2. a) Extinction coefficient (k) obtained from spectroscopic ellipsometry measurements for CuSCN, $PC_{70}BM$, mixed CuSCN:$PC_{70}BM$, and P3HT:$PC_{70}BM$ (reference) films. b) Maximum theoretical J_{SC} plot ($J_{SC,max}$, assuming 100% IQE) vs. active layer thickness simulated via transfer matrix calculations (device structure used for the simulations are shown in **Figure 1a**).

Furthermore, by employing the optical constants (refractive index, n and extinction coefficient, k) inferred from the ellipsometry measurements, we performed transfer-matrix (TM)

simulations[34-36] to estimate the maximum theoretical J_{SC} ($J_{SC,max}$) for bilayer CuSCN/$PC_{70}BM$ and mixed CuSCN:$PC_{70}BM$ solar cells. **Figure 2b** shows the $J_{SC,max}$ as a function of active-layer thickness. The results show that a J_{SC} > 10 mA cm^{-2} for both bilayer and mixed cells is achievable when the active-layer thickness is larger than 100 nm. When the thickness is between 50-150 nm, the $J_{SC,max}$ of a P3HT:$PC_{70}BM$ cell is higher than the bilayer and mixed cells, reaching a $J_{SC,max}$ of 13 mA cm^{-2} for a thickness of 100 nm. In practice, a maximum J_{SC} of 10-11 mA cm^{-2} has been reported for P3HT:$PC_{70}BM$ cells.[37] However, the device performance of such cells is limited by a low V_{OC} ≈ 0.6 V (compared to > 0.9 V in CuSCN:$PC_{70}BM$ cells) and a lower FF of 50-60% resulting in a PCE of 3-4%. It is worth noting that based on the $J_{SC,max}$ calculation, for an active-layer thickness larger than 150 nm, the $J_{SC,max}$ of the P3HT:$PC_{70}BM$ cell is comparable to that of the bilayer CuSCN/$PC_{70}BM$.

To compare the performance of the mixed CuSCN:$PC_{70}BM$ with bilayer CuSCN/$PC_{70}BM$ devices, both were fabricated using optimized conditions. Analysis of the saturation current (J_{SAT}), experimentally-measured short-circuit current (J_{SC}), and maximum theoretical J_{SC} ($J_{SC,max}$) can provide insight into the photogeneration and collection losses in the $PC_{70}BM$-based devices (see **Table 1**). Here, J_{SAT} is measured as the current reached when the solar cell is under strong reverse bias (-5 V); in this case nongeminate recombination is considered negligible and the current is limited by the photogeneration efficiency. Therefore, the ratio of J_{SAT} to $J_{SC,max}$ provides an estimation of the charge carrier generation efficiency (η_G), while the charge collection efficiency

(η_{coll}) can be calculated from the ratio of J_{SC} to J_{SAT}. As shown in **Table 1**, the J_{SC}, J_{SAT}, and $J_{SC,max}$ of the CuSCN:$PC_{70}BM$ cells are 7.6 mA cm^{-2}, 8.7 mA cm^{-2} and 10.0 mA cm^{-2}, respectively. The estimated charge carrier generation and charge collection efficiency are both almost 90%, indicating very efficient charge generation and collection in the mixed CuSCN:$PC_{70}BM$ solar cell. However, it is more difficult to estimate the J_{SAT} of the bilayer device as the current kept increasing with reverse bias. Thus, we used J_{SAT} at -5 V and obtained for the bilayer CuSCN/$PC_{70}BM$ cells a charge collection efficiency of less than 46%, while the charge generation exceeds 50% (**Table 1**). This indicates that both geminate and nongeminate recombinations are more pronounced in the bilayer cell than in the mixed cell.

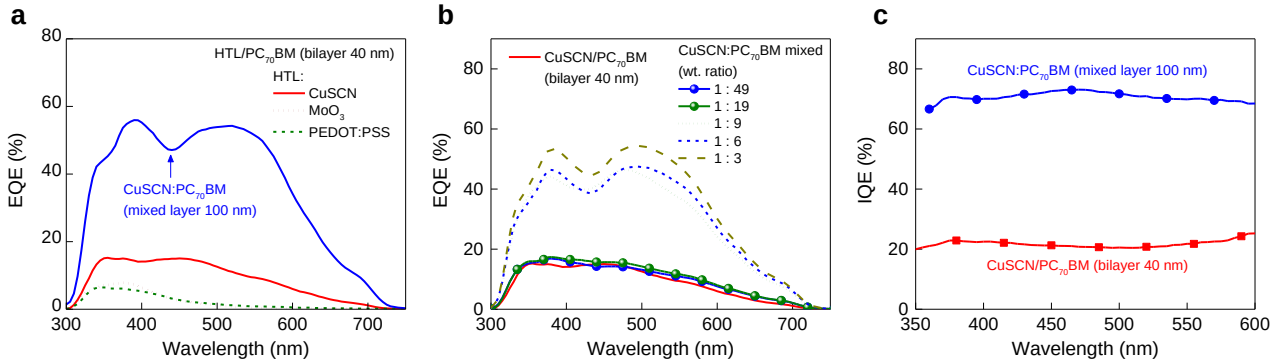

Figure 3. a) External quantum efficiency (EQE) spectra between 300 and 700 nm of the MoO_3/$PC_{70}BM$ and PEDOT:PSS/$PC_{70}BM$ devices compared to CuSCN-based cells (bilayer CuSCN/$PC_{70}BM$ and mixed layer CuSCN:$PC_{70}BM$ (weight ratio 1:3) cells). b) EQE spectra for mixed CuSCN:$PC_{70}BM$ solar cells of different weight ratios (1:49, 1:19, 1:9, 1:6, 1:3, and 1:2). The EQE of the best performing bilayer CuSCN/$PC_{70}BM$ is also shown for comparison. c) The internal quantum efficiency (IQE) spectra of the best performing bilayer CuSCN/$PC_{70}BM$ ($PC_{70}BM$ thickness 40 nm) and mixed CuSCN:$PC_{70}BM$ cells.

To determine the cause of the increased charge photogeneration in the CuSCN-based cells, the external quantum efficiency (EQE) was measured. A comparison of the EQE of bilayer cells obtained upon replacing CuSCN with MoO_3 or PEDOT:PSS is shown in **Figure 3a**. The EQE of MoO_3 or PEDOT:PSS-based cells are ≈7% and drop to almost zero at a wavelength of 550 nm (≈2.25 eV), which is close to the reported energy of the fullerene CT state (2.2-2.3 eV).[15, 20] This indicates that the photocurrent in the MoO_3 and PEDOT:PSS-based devices originates exclusively from intrinsic photogeneration of $PC_{70}BM$ through dissociation of loosely-bound intermolecular CT states.[15] In contrast, the EQE of the optimized CuSCN-based bilayer device exhibits a much higher EQE (≈15%) and a shift of the EQE cut-off from 550 nm to 730 nm (**Figure 3a**). CuSCN-based mixed layer device also shows a similar shape of the EQE spectra with a more pronounced maximum of EQE between 450-550 nm (**Figure 3b**). Yang et al.[22] and Zhang et al.[38] showed previously that in the case of fullerene-based Schottky-junction cells with low donor contents (5 wt% P3HT), the device photocurrent increased significantly compared to neat-$PC_{70}BM$ devices. Similarly, they also observed a shift of the EQE cut-off from 532 nm to 700 nm. They attributed the photocurrent enhancement across the entire spectrum (300-700 nm) to an increase in the dissociation efficiency of intermolecular CT states and intramolecular Frenkel excitons in $PC_{70}BM$ due to charge transfer to P3HT. Similarly, we argue that the dissociation of strongly-bound Frenkel excitons at the CuSCN/fullerene heterointerface (through the formation of a CT-like state) in CuSCN/$PC_{70}BM$ cells also contributes to the measured photocurrent, in addition to the

photocurrent from intramolecular CT states. It is noteworthy that the mixed layer CuSCN:$PC_{70}BM$ cells operate as *p-n* heterojunction devices, and not as Schottky-junction cells, which explains the significantly higher FF as compared to the Schottky-junction cells reported previously.[22, 38]

In general, increasing the amount of CuSCN in the mixture of $PC_{70}BM$ and CuSCN further improves the photocurrent (see **Figure 3c** and **Table S1**). The EQE for the CuSCN:$PC_{70}BM$ devices with ratios of 1:49 and 1:19 is ≈17%, not much improved compared to the optimized bilayer cell. The EQE further increases to ≈40%, when the ratio is 1:9 and exceeds 50% for CuSCN:$PC_{70}BM$ ratios in the range 1:3 to 1:2. The maximum of EQE at around 510 nm becomes more pronounced when the amount of CuSCN in the mixture increases. **Figure 3d** shows the internal quantum efficiency (IQE) spectra of the optimized bilayer and mixed layer cells (details on IQE measurements can be found in the Supporting information, **Figure S2**). Noticeably, the IQE of the optimized mixed layer cell is relatively high ≈70% across the visible spectrum suggesting efficient charge carrier generation and collection. In contrast, charge carrier recombination reduces the IQE (≈20%) in optimized bilayer cells (**Figure 3d**). The aforementioned IQEs are in agreement with those estimated from the J_{SC} divided by the $J_{SC,max}$ calculated by transfer matrix (**Table 1**) simulations, confirming the accuracy of our optical simulations.

Table 1. Summary of short-circuit current density (J_{SC}), saturated photocurrent density (J_{SAT}) estimated at -5 V, theoretical maximum photocurrent density ($J_{SC,max}$), charge generation efficiency (η_G), charge collection efficiency (η_{coll}), and estimated IQE ($J_{SC}/J_{SC,max}$).

	J_{SC} [mAcm^{-2}]	J_{SAT} [mAcm^{-2}]	$J_{SC,max}$ [mAcm^{-2}]	η_G [%]	η_{coll} [%]	*IQE* [%]
CuSCN/$PC_{70}BM$ (40 nm)	1.83	4.0[a)]	7.9	50[b)]	46[c)]	23
CuSCN:$PC_{70}BM$ (100 nm)	7.60	8.7	10.0	87.0	87.0	76

FF of the bilayer device is low therefore correct value of J_{SAT} cannot be obtained. Thus: [a)] $J_{SAT} > 4$ mAcm^{-2}; [b)] $\eta_G = J_{SAT}/J_{SC,max} > 50\%$; [c)] $\eta_{coll} = J_{SC}/J_{SAT} < 46\%$.

To further investigate the nature of charge photogeneration and recombination in $PC_{70}BM$ and CuSCN:$PC_{70}BM$ devices after optical excitation, we performed time-delayed collection field (TDCF) experiments. The devices were subjected to variable pre-biases (V_{pre}, between -1.0 and 1.0 V) and a short delay of 10 ns prior to the application of a collection bias (V_{col} = -4 V). The transient photocurrent was integrated to determine the total amount of collected charges (Q_{tot}). Excitation was performed at a wavelength of 532 nm, and the pulse fluence used here was 0.1 µJ cm^{-2} (only for the MoO_3/$PC_{70}BM$ device, the pulse fluence used was 0.2 µJ cm^{-2} to improve the signal-to-noise ratio, **Figure S3**). The laser pulse fluences were in the linear regime (0.05-0.9 µJ cm^{-2}) of the photocurrent response to ensure negligible nongeminate recombination prior to extraction (**Figure S4**).[39] The total number of generated charges Q_{tot} (defined as the integral over the entire current transient) for different values of V_{pre} is shown in **Figure 4a** for MoO_3/$PC_{70}BM$, bilayer CuSCN/$PC_{70}BM$, and mixed-phase CuSCN:$PC_{70}BM$ devices. **Figure 4a** indicates that Q_{tot} does not depend on the applied pre-bias, but stays rather constant across the entire range of prebias investigated. Interestingly, the TDCF measurement of a bilayer CuSCN/$PC_{70}BM$ device (**Figure**

4a) shows a weak dependence of charge collection on V_{pre}. Geminate losses at open-circuit condition are approximately 20% higher than the losses incurred at -1 V (**Figure 4b**).

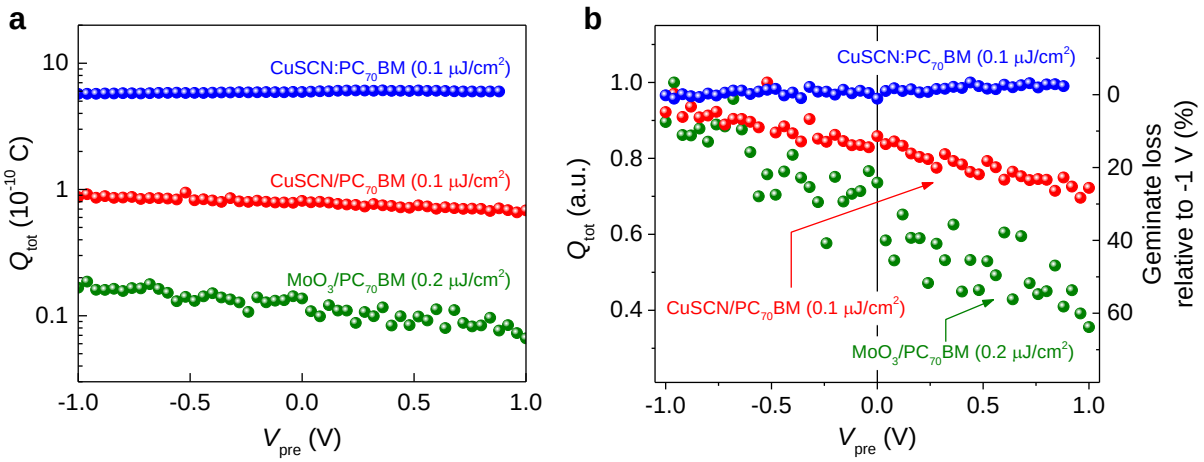

Figure 4. a) Total extracted charge (Q_{tot}) as a function of pre-bias (V_{pre}) measured by time delayed collection field (TDCF) experiments using a 10 ns delay time between excitation and extraction, a -4 V collection bias, and a laser pulse fluence of 0.1 μJ cm^{-2} (0.2 μJ cm^{-2} for MoO_3/$PC_{70}BM$ devices). (b) The same data normalized to Q_{tot} at -1 V. The right axis indicates the percentage of photogenerated carriers lost due to geminate recombination relative to the loss incurred at -1 V.

For a MoO_3/$PC_{70}BM$ device, the field-dependence of charge generation is even stronger with geminate losses approximately 60% higher at open-circuit condition than incurred at -1 V. This finding is consistent with the observation by Hahn et al.,[15] that the intrinsic photocurrents in single-layer C_{60} and $PC_{60}BM$ solar cell devices (ITO/MoO_3/C_{60} or $PC_{60}BM$/Al) are field-dependent. The difference in the field-dependence of total extracted charge seen in MoO_3/$PC_{70}BM$, bilayer CuSCN/$PC_{70}BM$, and mixed CuSCN:$PC_{70}BM$ (**Figure 4**) devices is therefore clear evidence that a greater proportion of the photocurrent in the CuSCN-based devices results from

the dissociation of photogenerated intramolecular excitons and charge transfer at the CuSCN-$PC_{70}BM$ interface. This picture is consistent with the subgap-EQE data shown in **Figure S5**. Extended absorption tails for photon energies below 1.65 eV was observed in the case of bilayer CuSCN/$PC_{70}BM$ and mixed phase CuSCN:$PC_{70}BM$ devices, while it was absent in the EQE of the MoO_3/$PC_{70}BM$ device. We attribute this absorption tail to CT states present at the CuSCN-$PC_{70}BM$ interface. Note that the CT absorption appears to be more pronounced in the case of mixed layer devices, indicating a larger CuSCN-$PC_{70}BM$ interface area. The change in the interfacial area is also manifested as a decrease in the V_{OC} in mixed layer cells when the amount of CuSCN in the mixed active layer is increased (from 0.96 V for ratio 1:49 to 0.92 V for ratio 1:2, **Table S1**). This is in agreement with the results of Vandewal et al. obtained on fullerene-based devices with low donor content, which showed that the V_{OC} can be tuned independently of interfacial energetics and depends on the interfacial area available for charge carrier recombination.[40]

Next, we compared the recombination kinetics by determining the second order nongeminate recombination coefficients (k_{BMR}) from the TDCF measurements. A much higher intensity (fluence of 4.8 μJ/cm^2) was used for this measurement, in the regime where the relation between light intensity and collected charges is non-linear (**Figure S4**). Here, the recombination coefficients k_{BMR} are determined from the amount of charge left in the device (Q_{col}) as a function of the delay time after photoexcitation.[39] Photocurrents were measured for a fixed collection

voltage (V_{col} = -4 V) and a pre-bias (V_{pre}) close to the V_{OC} of the devices (0.98 V for bilayer cell and 0.9 V for mixed cell). As V_{pre} is close to open-circuit conditions, charge carriers remain in the device for a sufficiently long time to undergo nongeminate recombination. Therefore, a decrease in the total charge extracted as a function of the delay time, as apparent from **Figure 5**, is indicative of the recombination of free charge carriers.

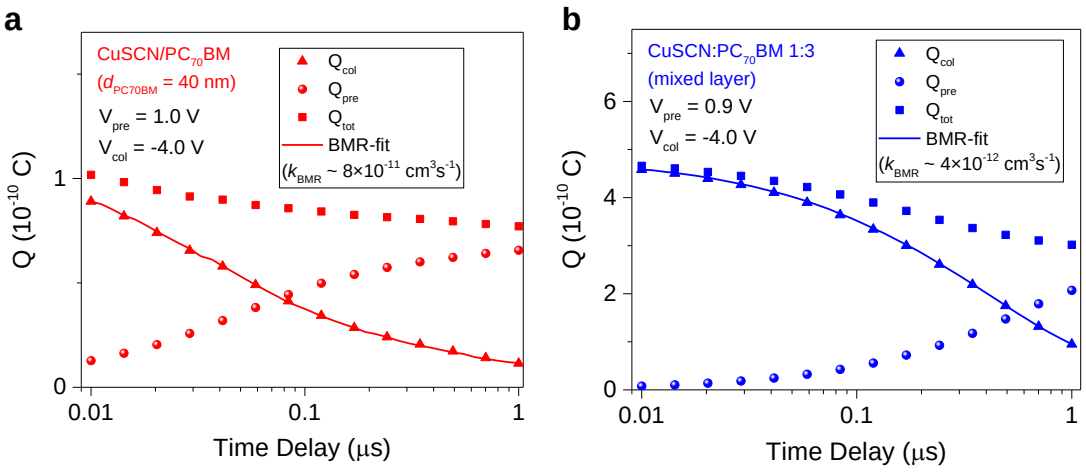

Figure 5. Plots of Q_{pre} (t_d), Q_{col}(t_d), and Q_{tot} (t_d) as determined from TDCF transients recorded for a prebias close to V_{OC} as a function of delay time (t_d) for a) bilayer CuSCN/$PC_{70}BM$ devices (40 nm) and b) mixed CuSCN:$PC_{70}BM$ devices. The collection bias was -4V. Fits to second order (nongeminate) recombination dynamics (solid lines) are also shown. The second order recombination rate constant (k_{BMR}) of the bilayer and mixed cells are denoted in the legend (Laser pulse fluence: 4.8 µJ/cm^2).

We were able to iteratively fit the measured values of Q_{col} for the bilayer and mixed cells according to the report by Kniepert et al.[39] In that way we obtain second order nongeminate recombination coefficients of (k_{BMR}) 8 × 10^{-11} cm^3 s^{-1} for bilayer CuSCN/$PC_{70}BM$ devices and 6 × 10^{-11} cm^3 s^{-1} for MoO_3/$PC_{70}BM$ devices (**Figure S6**), whereas for mixed CuSCN:$PC_{70}BM$ solar

cells the k_{BMR} is more than one order of magnitude lower ($\approx 4 \times 10^{-12}$ cm^3 s^{-1}). The k_{BMR} of the mixed CuSCN:$PC_{70}BM$ is notably low in comparison with the coefficient reported for optimized P3HT:$PC_{70}BM$ devices (5×10^{-12} cm^3 s^{-1}) that also show high FFs of over 60%.[39]

3. Conclusion

We have elucidated the origin of the significantly enhanced performance of mesostructured CuSCN-nanowire:$PC_{70}BM$ solar cells as compared to planar bilayer CuSCN/$PC_{70}BM$ devices. The combination of a range of complementary characterization techniques revealed that the performance improvements observed in this new type of mesostructured CuSCN-nanowire:$PC_{70}BM$ solar cells result primarily from: (i) improved charge generation and collection efficiency from approximately 50%, in planar bilayer cells, to nearly 90% in mesostructured cells; (ii) reduced geminate recombination losses; and (iii) reduced nongeminate recombination. We were also eble to establish that a greater proportion of the photocurrent in the CuSCN-based cells results from the efficient dissociation of photogenerated excitons and charge transfer at the CuSCN-$PC_{70}BM$ heterointerface. We hypothesize that this new CuSCN/photocactive material-based solar cell concept should be transferable to a wider range of organic as well as inorganic materials with more appropriate absorption characteristics, thereby further increasing the efficiency of the solar cells. Finally, our study lay the foundation for an improved understanding

of carrier photogeneration within the acceptor phase of BHJ organic solar cells, which up to now has been largely ignored.

Experimental Section

Solar cell fabrication: Indium tin oxide (ITO) coated glass substrates (Kintec Company, 10 Ω/sq.) were cleaned by sequential ultra-sonication in dilute Extran 300 detergent solution, deionized water, acetone and isopropyl alcohol for 20 min each. These substrates were then cleaned by UV-ozone treatment for 30 min. For the PEDOT:PSS/$PC_{70}BM$ cells, a thin layer (~30 nm) of PEDOT:PSS was spin-cast onto the UV-ozone cleaned substrates, dried on a heating plate at 120 °C for 10 min. For the MoO_3/$PC_{70}BM$ cells, a thin layer (~16 nm) of MoO_3 was deposited by thermal evaporation under high vacuum (5×10^{-6} mbar). The PEDOT-coated and MoO_3-coated substrates were then transferred into a dry nitrogen glove box (< 3 ppm O2). $PC_{70}BM$ layer (20 mg/ml in chlorobenzene) were then spun at 2000 rpm for 30 s (active-layer thickness 30 nm). After the spin-coating step, all substrates were transferred into a vacuum chamber. A layer of 10 nm bathocuproine (BCP) (Sigma-Aldrich) followed by a 100 nm of aluminium were then thermally evaporated at 5×10^{-6} mbar to complete the device fabrication. More details on the fabrication of the CuSCN-based devices (bilayer CuSCN/$PC_{70}BM$ and mixed layer CuSCN:$PC_{70}BM$ cells) can be found elsewhere [7].

High resolution TEM (HR-TEM) analysis: Details on sample preparation and data acquisition for the HR-TEM analysis have been reported previously [7].

Dynamic secondary-ion mass spectrometry (D-SIMS): Depth profiling experiments were performed on a Dynamic SIMS instrument from Hiden Analytical Company (Warrington-UK) operated under ultra-high vacuum conditions, typically 10^{-9} torr. A continuous Ar^+ ion beam was employed at an energy of 2 keV to sputter the surface while the selected emitted ions ascribed to C_2, S, SCN, InO, CuO were sequentially collected using a MAXIM spectrometer equipped with a quadrupole analyzer. The raster of the sputtered area is estimated to be 500 × 500 μm^2. In order to avoid the edge effect during depth profiling experiments, it is necessary to acquire data from a small area located in the middle of the eroded region. Using an adequate electronic gating, the acquisition area from which the depth profiling data were extracted was approximately 50 × 50 μm^2. Assuming a constant sputter rate, the conversion of sputtering time to sputtering depth scales was carried out by measuring the depth of the crater generated at the end of the depth profiling experiment using a stylus profiler from Veeco.

Transfer-matrix simulation: Transfer matrix modeling was used to simulate the maximum theoretical J_{SC} plots as a function of active layer thickness (thickness range: 0-500 nm) and

electromagnetic field intensity profile $|E|^2$ of the device stack; the model assumes 100% internal quantum efficiency (IQE). The transfer matrix code for these simulations was developed by George F. Burkhard and Eric T. Hoke; code available from: transfermatrix/index.html. The optical constants *n* and *k* for the active layers were collected by variable angle spectroscopic ellipsometry (VASE) with an M-2000 ellipsometer (J.A. Woolam Co., Inc). The active layers were cast on clean silicon substrates coated with SiO_2 (90 nm or 120 nm). The VASE measurements were performed with incident angles being varied from 45 to 75° in steps of 5° relative to the samples.

Solar cell characterization*:* Solar-cell characterization has been performed inside a glovebox using a Keithley 2400 source meter in the dark and under illumination by a simulated 100 mW cm^{-2} AM1.5G light source using Oriel Sol3A Class AAA solar simulator calibrated to 1 sun, AM1.5G, with a KG-5 silicon reference cell certified by Newport. CV measurements were performed in dark in the glovebox using a Solartron 1260A Impedance Analyzer.

Time delayed collection field (TDCF) measurement: The home-built TDCF setup uses the second harmonic (532 nm) of an actively Q-switched sub-ns Nd:YVO4 laser (INNOLAS piccolo AOT) operating at a repetition rate of 5 kHz as excitation source. To minimize the RC response time, a small device area of 1 mm^2 is used in TDCF experiments. The samples were measured under dynamic vacuum conditions to avoid any degradation. A Keysight S1160A function generator was

used to provide the pre-bias and extraction bias pulses, while a Keysight four channel digital oscilloscope (Infiniivision MSOX3034T) was used to measure the current response of the device.

External quantum efficiency (EQE) measurement: EQE was characterized using a specially designed EQE system (PV measurement Inc.). Measurements were performed at zero bias by illuminating the device with monochromatic light supplied from a Xenon arc lamp in combination with a dual-grating monochromator. The number of photons incident on the sample was calculated for each wavelength by using a silicon photodiode calibrated by NIST.

Subgap EQE measurement: The EQE spectra were collected under short-circuit bias conditions under focused monochromatic illumination generated by a monochromator (Newport 74125) equipped with a 400 W Xenon arc lamp (Newport 66902). The monochromatic light beam was modulated by an optical chopper (275 Hz). The device output current was measured as a function of incident photon energy using a lock-in amplifier (Stanford Instruments SR 830), while the lamp intensity was calibrated using Ge and Si photodiodes.

UV-Vis-spectroscopy*:* Steady-state absorption measurements were performed using a Cary 5000 UV-visible spectrometer (Agilent Technologies).

Supporting Information

Supporting Information is available from the Wiley Online Library or from the authors.

Acknowledgements

Y.F. and A.S. contributed equally to this work. The authors acknowledge the King Abdullah University of Science and Technology (KAUST) for the financial support.

Received: ((will be filled in by the editorial staff))
Revised: ((will be filled in by the editorial staff))
Published online: ((will be filled in by the editorial staff))

References:

[1] W. C. Zhao, S. S. Li, H. F. Yao, S. Q. Zhang, Y. Zhang, B. Yang, J. H. Hou, J. Am. Chem. Soc. 2017, 139, 7148.
[2] Z. Fei, F. D. Eisner, X. Jiao, M. Azzouzi, J. A. Röhr, Y. Han, M. Shahid, A. S. R. Chesman, C. D. Easton, C. R. McNeill, T. D. Anthopoulos, J. Nelson, M. Heeney, Adv. Mater., 1705209.
[3] W. C. Zhao, D. P. Qian, S. Q. Zhang, S. S. Li, O. Inganas, F. Gao, J. H. Hou, Adv. Mater. 2016, 28, 4734.
[4] H. J. Bin, L. Gao, Z. G. Zhang, Y. K. Yang, Y. D. Zhang, C. F. Zhang, S. S. Chen, L. W. Xue, C. Yang, M. Xiao, Y. F. Li, Nat Commun 2016, 7, 13651.
[5] Z. K. Li, K. Jiang, G. F. Yang, J. Y. L. Lai, T. X. Ma, J. B. Zhao, W. Ma, H. Yan, Nat Commun 2016, 7, 13094.
[6] S. S. Chen, Y. H. Liu, L. Zhang, P. C. Y. Chow, Z. Wang, G. Y. Zhang, W. Ma, H. Yan, J. Am. Chem. Soc. 2017, 139, 6298.
[7] W.-Y. Sit, F. D. Eisner, Y.-H. Lin, Y. Firdaus, A. Seitkhan, A. H. Balawi, F. Laquai, C. H. Burgess, M. A. McLachlan, G. Volonakis, F. Giustino, T. D. Anthopoulos, Adv Sci, 1700980.
[8] T. D. Anthopoulos, C. Tanase, S. Setayesh, E. J. Meijer, J. C. Hummelen, P. W. M. Blom, D. M. de Leeuw, Adv. Mater. 2004, 16, 2174.
[9] A. K. K. Kyaw, D. H. Wang, H. R. Tseng, J. Zhang, G. C. Bazan, A. J. Heeger, Appl. Phys. Lett. 2013, 102, 163308

[10] Y. J. He, Y. F. Li, Phys. Chem. Chem. Phys. 2011, 13, 1970.
[11] B. C. Thompson, J. M. J. Frechet, Angew. Chem. Int. Ed. 2008, 47, 58.
[12] S. D. Dimitrov, C. B. Nielsen, S. Shoaee, P. S. Tuladhar, J. P. Du, I. McCulloch, J. R. Durrant, J. Phys. Chem. Lett. 2012, 3, 140.
[13] G. F. Burkhard, E. T. Hoke, Z. M. Beiley, M. D. McGehee, J. Phys. Chem. C 2012, 116, 26674.
[14] S. D. Dimitrov, Z. G. Huang, F. Deledalle, C. B. Nielsen, B. C. Schroeder, R. S. Ashraf, S. Shoaee, I. McCulloch, J. R. Durrant, Energy Environ. Sci. 2014, 7, 1037.
[15] T. Hahn, S. Tscheuschner, C. Saller, P. Strohriegl, P. Boregowda, T. Mukhopadhyay, S. Patil, D. Neher, H. Bassler, A. Kohler, J. Phys. Chem. C 2016, 120, 25083.
[16] A. Armin, I. Kassal, P. E. Shaw, M. Hambsch, M. Stolterfoht, D. M. Lyons, J. Li, Z. G. Sho, P. L. Burn, P. Meredith, J. Am. Chem. Soc. 2014, 136, 11465.
[17] M. M. Wienk, J. M. Kroon, W. J. H. Verhees, J. Knol, J. C. Hummelen, P. A. van Hal, R. A. J. Janssen, Angew. Chem. Int. Ed. 2003, 42, 3371.
[18] S. Jeglinski, Z. V. Vardeny, D. Moses, V. I. Srdanov, F. Wudl, Synth. Met. 1992, 50, 557.
[19] C. Keiderling, S. Dimitrov, J. R. Durrant, J. Phys. Chem. C 2017, 121, 14470.
[20] S. Kazaoui, R. Ross, N. Minami, Phys. Rev. B 1995, 52, 11665.
[21] P. C. Y. Chow, S. Albert-Seifried, S. Gelinas, R. H. Friend, Adv. Mater. 2014, 26, 4851.
[22] B. Yang, F. W. Guo, Y. B. Yuan, Z. G. Xiao, Y. Z. Lu, Q. F. Dong, J. S. Huang, Adv. Mater. 2013, 25, 572.
[23] J. J. Benson-Smith, H. Ohkita, S. Cook, J. R. Durrant, D. D. C. Bradley, J. Nelson, Dalton Trans. 2009, 10000.
[24] S. Cook, H. Ohkita, J. R. Durrant, Y. Kim, J. J. Benson-Smith, J. Nelson, D. D. C. Bradley, Appl. Phys. Lett. 2006, 89.
[25] J. S. Huang, Y. Yang, Appl. Phys. Lett. 2007, 91.
[26] N. Wijeyasinghe, T. D. Anthopoulos, Semicond. Sci. Technol. 2015, 30.
[27] N. Wijeyasinghe, A. Regoutz, F. Eisner, T. Du, L. Tsetseris, Y.-H. Lin, H. Faber, P. Pattanasattayavong, J. Li, F. Yan, M. A. McLachlan, D. J. Payne, M. Heeney, T. D. Anthopoulos, Adv. Funct. Mater. 2017, 27, 1701818.
[28] G. Garcia-Belmonte, A. Munar, E. M. Barea, J. Bisquert, I. Ugarte, R. Pacios, Org. Electron. 2008, 9, 847.
[29] Y. Firdaus, L. P. Maffei, F. Cruciani, M. A. Muller, S. J. Liu, S. Lopatin, N. Wehbe, G. O. N. Ndjawa, A. Amassian, F. Laquai, P. M. Beaujuge, Adv. Energy Mater. 2017, 7, 1700834.
[30] M. Kim, J. Lee, S. B. Jo, D. H. Sin, H. Ko, H. Lee, S. G. Lee, K. Cho, J. Mater. Chem. 2016, 4, 15522.
[31] B. F. Xue, B. Vaughan, C. H. Poh, K. B. Burke, L. Thomsen, A. Stapleton, X. J. Zhou, G. W. Bryant, W. Belcher, P. C. Dastoor, J. Phys. Chem. C 2010, 114, 15797.

[32] F. J. Zhang, Z. L. Zhuo, J. Zhang, X. Wang, X. W. Xu, Z. X. Wang, Y. S. Xin, J. Wang, J. Wang, W. H. Tang, Z. Xu, Y. S. Wang, Sol. Energy Mater. Sol. Cells 2012, 97, 71.
[33] G. Orlandi, F. Negri, Photochemical & Photobiological Sciences 2002, 1, 289.
[34] L. A. A. Pettersson, L. S. Roman, O. Inganas, J Appl Phys 1999, 86, 487.
[35] P. Peumans, A. Yakimov, S. R. Forrest, J Appl Phys 2003, 93, 3693.
[36] G. F. Burkhard, E. T. Hoke, M. D. McGehee, Adv. Mater. 2010, 22, 3293.
[37] D. H. Wang, J. K. Kim, J. H. Seo, O. O. Park, J. H. Park, Sol. Energy Mater. Sol. Cells 2012, 101, 249.
[38] M. L. Zhang, H. Wang, H. K. Tian, Y. H. Geng, C. W. Tang, Adv. Mater. 2011, 23, 4960.
[39] J. Kniepert, M. Schubert, J. C. Blakesley, D. Neher, J. Phys. Chem. Lett. 2011, 2, 700.
[40] K. Vandewal, J. Widmer, T. Heumueller, C. J. Brabec, M. D. McGehee, K. Leo, M. Riede, A. Salleo, Adv. Mater. 2014, 26, 3839.

Charge photogeneration and recombination in mesostructured CuSCN-nanowire/$PC_{70}BM$ solar cells

Yuliar Firdaus, Akmaral Seitkhan, Flurin Eisner, Wai-Yu Sit, Zhipeng Kan, Nimer Wehbe, Ahmed H. Balawi, Emre Yengel, Safakath Karuthedath, Frédéric Laquai, Thomas D. Anthopoulos**

Keywords: Solar cells; Copper (I) thiocyanate; PCBM; charge photogeneration, charge recombination

Efficient charge photogeneration and collection is realized in solar cells based on a mixture of copper(I)thiocyanate (CuSCN) and $PC_{70}BM$ acting as the hole-extracting and light-absorbing materials, respectively. Our study reveals that the mesostructured *p-n* heterointerface formed spontenously between CuSCN and $PC_{70}BM$ facilitates efficient charge dissociation of charge-transfer states created upon illumination. In parallel, the interface allows strictly selective charge collection prior to recombination.

ToC Graphic

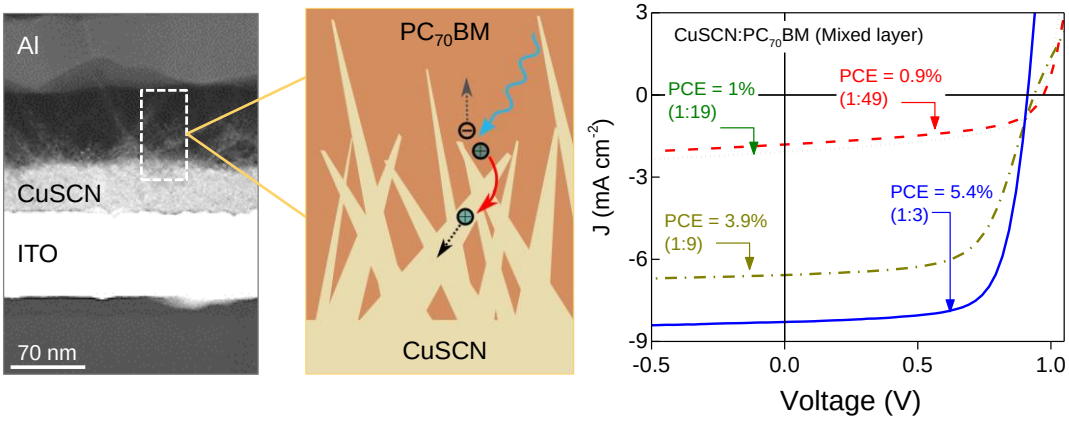

Supporting Information

Charge photogeneration and recombination in mesostructured CuSCN-nanowire/ $PC_{70}BM$ solar cells

Yuliar Firdaus, Akmaral Seitkhan, Flurin Eisner, Wai-Yu Sit, Zhipeng Kan, Nimer Wehbe, Ahmed H. Balawi, Emre Yengel, Safakath Karuthedath, Frédéric Laquai, Thomas D. Anthopoulos**

Table S1. Solar cell performance dependence on the $PC_{70}BM$ thickness for bilayer cells (top table) and the performance dependence on the CuSCN:$PC_{70}BM$ ratio of mixed layer cells for two different total solid concentrations (bottom table).

Active layer		V_{oc} [V]	J_{sc} [mA cm^{-2}]	*FF* [%]	*PCE* [%]
Bilayer ($PC_{70}BM$ 40 nm)					
CuSCN/$PC_{70}BM$		0.98 ± 0.03	1.8 ± 0.24	48 ± 3.2	0.84 ± 0.12
MoO_3/$PC_{70}BM$		0.81 ± 0.08	0.2 ± 0.005	37 ± 2.8	0.07 ± 0.01
PEDOT:PSS/$PC_{70}BM$		0.95 ± 0.03	0.3 ± 0.01	30 ± 1.2	0.08 ± 0.01
CuSCN:$PC_{70}BM$ (mixed layer)					
Total solid: 40 mg/ml	1:49	0.96 ± 0.020	1.8 ± 0.08	49 ± 2.9	0.84 ± 0.08
	1:19	0.94 ± 0.014	2.1 ± 0.06	50 ± 2.7	1.00 ± 0.05
	1:9	0.93 ± 0.010	6.5 ± 0.03	61 ± 2.6	3.70 ± 0.21
	1:5	0.92 ± 0.008	7.0 ± 0.11	71 ± 1.2	4.60 ± 0.12
	1:3	0.91 ± 0.005	7.9 ± 0.11	71 ± 1.9	5.10 ± 0.17
	1:2	0.92 ± 0.008	7.9 ± 0.08	67 ± 3.1	4.80 ± 0.16

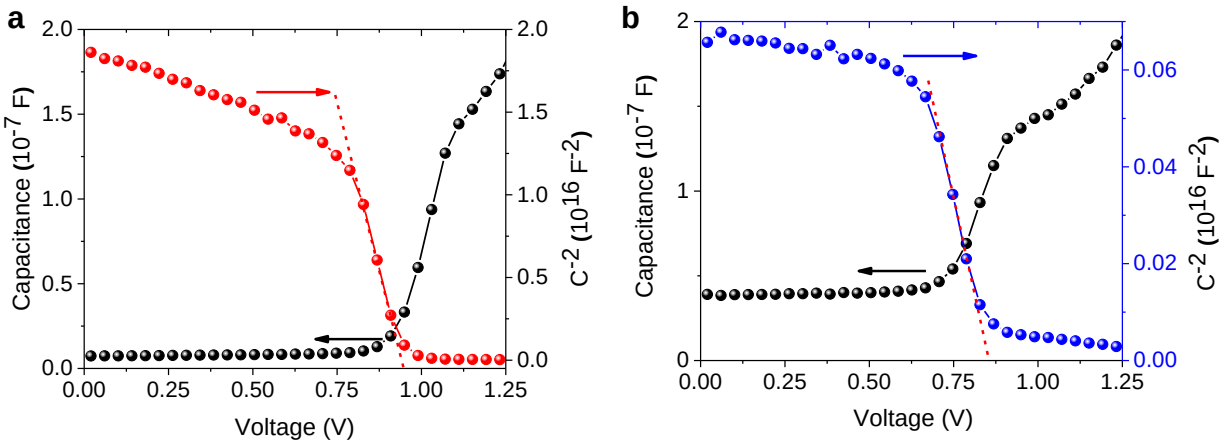

Figure S1. Analysis of Mott-Schottky curves (1 KHz) for the optimized: a) bilayer CuSCN/$PC_{70}BM$ cell and b) mixed layer CuSCN:$PC_{70}BM$. Based on the curves, charge carrier density, *n*, is calculated as 8.75 x 10^{15} cm^{-3} with the build-in voltage, V_{bi} = 0.96 V and 44 x 10^{15} cm^{-3} with the V_{bi} = 0.88 V for bilayer and mixed cells, respectively.

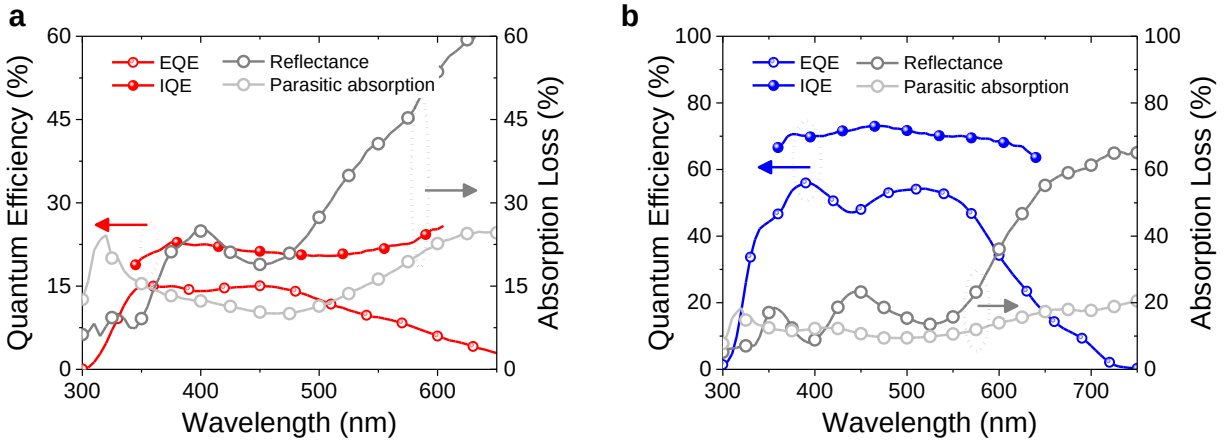

Figure S2. EQE, IQE, reflectance and parasitic absorption of optimized: (a) bilayer CuSCN/$PC_{70}BM$ (40 nm) device, and (b) mixed layer CuSCN:$PC_{70}BM$ device.

The internal quantum efficiency (IQE) of optimized bilayer CuSCN/$PC_{70}BM$ and mixed layer CuSCN:$PC_{70}BM$ was calculated from **Eq. S1**: ``

$$IQE = EQE/(1 - R\% - ParasiticAbsorption) \quad \text{(S1)}$$

The EQE spectra were collected from optimized devices. The reflectance (R%) spectra were collected with the integrating sphere using the same EQE system. The parasitic absorption was obtained from transfer matrix modeling.

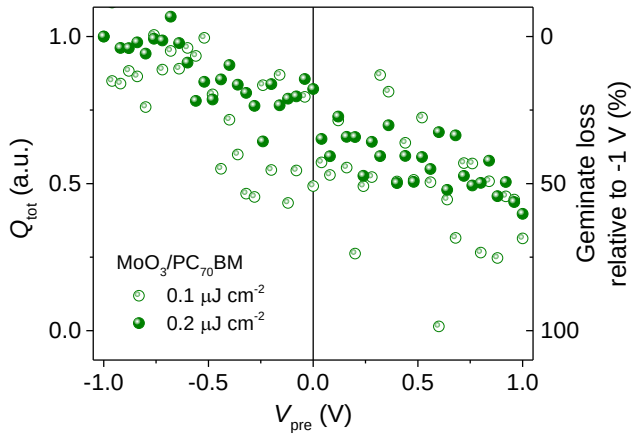

Figure S3. Total extracted charge data normalized to Q_{tot} at -1 V of $MoO_3/PC_{70}BM$ device for different laser pulse fluence (0.1 and 0.2 μJ cm^{-2}).

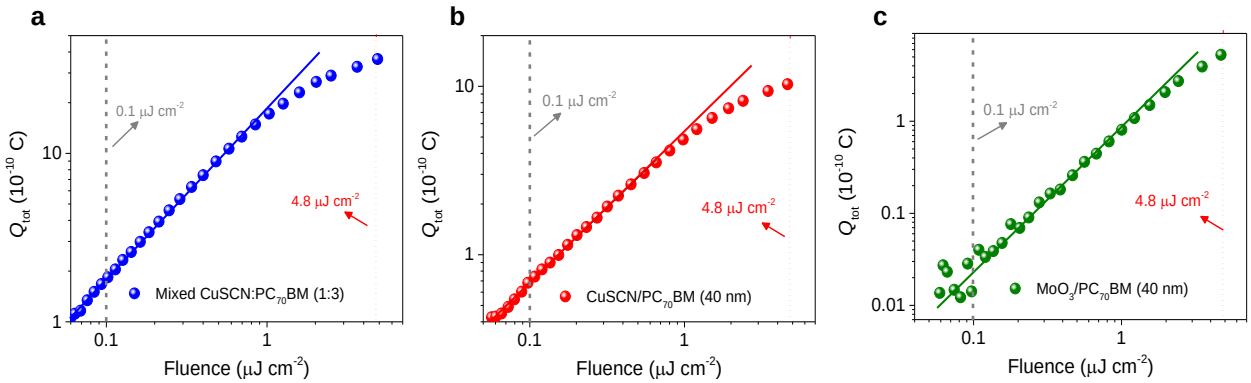

Figure S4. Dependence of the extracted charge (Q_{tot}) on the laser pulse fluence, using a 10-ns delay time and -4 V as the collection bias, for optimized: (a) mixed layer CuSCN:$PC_{70}BM$, (b) bilayer CuSCN/$PC_{70}BM$, and (c) $MoO_3/PC_{70}BM$ devices. The dashed lines mark the pulse fluence used for the V_{pre} sweep measurements (low fluence, 0.1 μJ cm^{-2})and dotted lines mark the fluence used for the time delay (t_{del}) sweep measurements (high fluence, 4.8 μJ cm^{-2}). Solid lines: fits to the data.

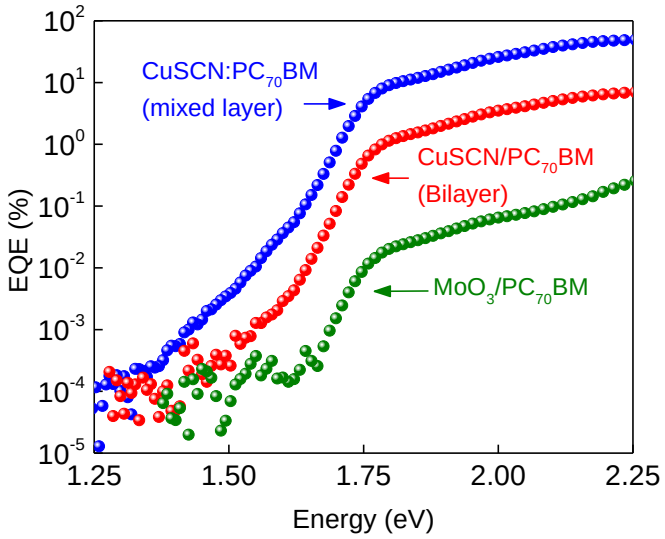

Figure S5. The sub-bandgap EQE spectra of the optimized MoO_3/$PC_{70}BM$, bilayer CuSCN/$PC_{70}BM$ and CuSCN:$PC_{70}BM$ devices. The EQE showing the absorption tail of the bilayer and mixed layer cells in comparison to MoO_3/$PC_{70}BM$ device.

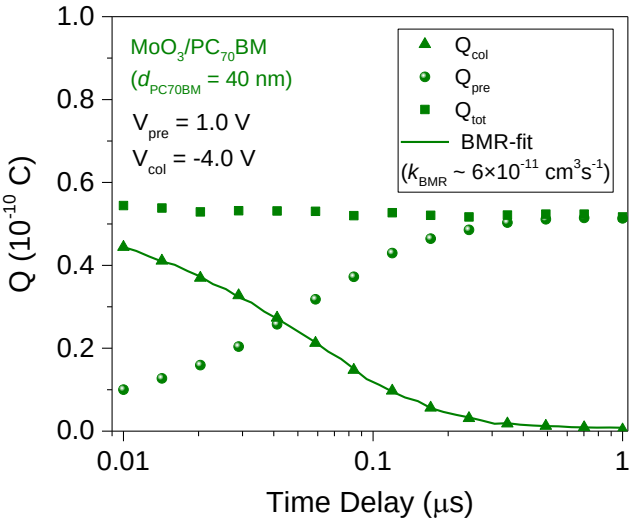

Figure S6. Plots of Q_{pre} (t_d), Q_{col}(t_d), and Q_{tot} (t_d) as determined from TDCF transients recorded for a prebias near V_{OC} as a function of delay time (t_d) for MoO_3/$PC_{70}BM$ device (40 nm). The collection voltage is -4V and corresponding bimolecular recombination (BMR) fits (solid lines) are also shown. The recombination rate constant (k_{BMR}) of the bilayer and mixed cells are denoted in legend (Laser pulse fluence: 4.8 μJ/cm^2).